Electronic Supplementary Information from:

Searching for kagome multi-bands and edge states in a predicted organic topological insulator

By L. Hernández-López et al.

This document contains the following items:

- The Methods section consisting of sample preparation, experimental and theoretical details.

- 11 Supplementary figures.

- Supplementary References

METHODS

Sample preparation. All the experiments were performed under ultra-high vacuum conditions. The Cu(111) single crystal was prepared by repeated cycles of Ar^+ sputtering at 1.0 kV and annealing at 720 K in a preparation chamber with a base pressure below $5 \cdot 10^{-10}$ mbar. DCA molecules are evaporated from a Knudsen cell by thermal evaporation at a rate ~0.03 ML/min on a substrate at RT. The network forms spontaneously by self-assembly.

STM/STS details. Two low-temperature STMs (LT-STM) were used to characterize topography, point spectroscopy (STS) and high-resolution topography (CO-functionalized tip measurements). These are located in chambers with a base pressure better than $2 \cdot 10^{-10}$ mbar and operate at 4 K. A W tip was used in all cases. All the voltages are referred to the sample. Common topography images were acquired with constant current mode, while the functionalized tip images were recorded at constant height mode. These images were afterwards treated by Laplacian filtering to obtain bond resolution. STS measurements were performed at constant height (defined by the set point I_t = 80pA; V_{bias}= -1V) sweeping the bias with the lock-in technique. Presented spectra are averaged over 4 or 5 equivalent points obtained from a single grid of spectroscopy.

ARPES details. The data presented was acquired at the APE beamline of the Elettra Sincrotrone Trieste using linearly polarized light. The photon energy was varied from 40 to 16 eV and the best signal-to-noise ratio was found at 18 eV. The temperature used for ARPES acquisition was 78 K, and we used a deflector type analyser that provided an overall energy and angle resolution better than 30 meV and 0.1°. We detected beam damage with expositions over 45 minutes (signal reduction to 75% of the initial intensity on the adatom band located at -0.6 eV), so the sample was continuously moved to find fresh spots.

Prior to the synchrotron measurements, the network was probed with a lab-based experimental setup using a display-type hemispherical electron analyzer (SPECS Phoibos 150, energy/angle resolution of 50 meV/0.1°) combined with a monochromatized Helium I source (hv=21.2 eV). Measurements were acquired with the sample at 150 K by moving the polar angle. The band structure measured in this other setup was identical to the synchrotron and no beam damage was detected.

Details of the tight binding calculations. On the main text, we referred to tight binding calculations for a finite-sized ribbon of a kagome lattice. We have adapted the theory developed

in Ref. [S1], where the Hamiltonian was composed of two contributions: the first one taking into account nearest-neighbor hopping (measured with the parameter t), and the second one tracking the effects of the nearest-neighbor intrinsic SOC (via the parameter λ). Modifying the ratio λ/t allows one to evolve the system from topologically trivial (when $\lambda = 0$) to topologically nontrivial (for sufficiently strong SOC). The kagome lattice is associated with a three particle basis, which can be labelled A, B, and C. In order to see the effects of symmetry breaking, we use different hopping parameters between each of the molecular sites, leading to the three distinct hopping parameters t_{AB}, t_{BC}, and t_{CA}. For a semi-infinite kagome lattice (infinite in the x-direction and finite in the y-direction), k_x is a good quantum number along the formed ribbon. Carrying out the numerical diagonalization of the Hamiltonian for a kagome ribbon of width N leads to 3N eigenenergies in the first Brillouin zone (defined by $k_x \in [-\frac{\pi}{d}, \frac{\pi}{d}]$).

We present our tight-binding results in Fig. S11 of this Supplementary Material for the kagome lattice. In going from left to right across the rows of Fig. S11, we successively increase the SOC strength. This allows one to see topologically trivial bandstructures towards the left hand side of the figure, and the evolution into topological nontriviality towards the right hand side. The very top row represents the symmetric case with equal hopping ($t_{AB} = t_{BC} = t_{CA} = t$) and is used as a reference. The influence of symmetry breaking is displayed in the second and third highest rows of Fig. S11, where $t_{AB} \neq t_{BC} = t_{CA}$ and $t_{AB} \neq t_{BC} \neq t_{CA}$ respectively, which mimics the effects of network imperfections.

SUPPLEMENTARY FIGURES

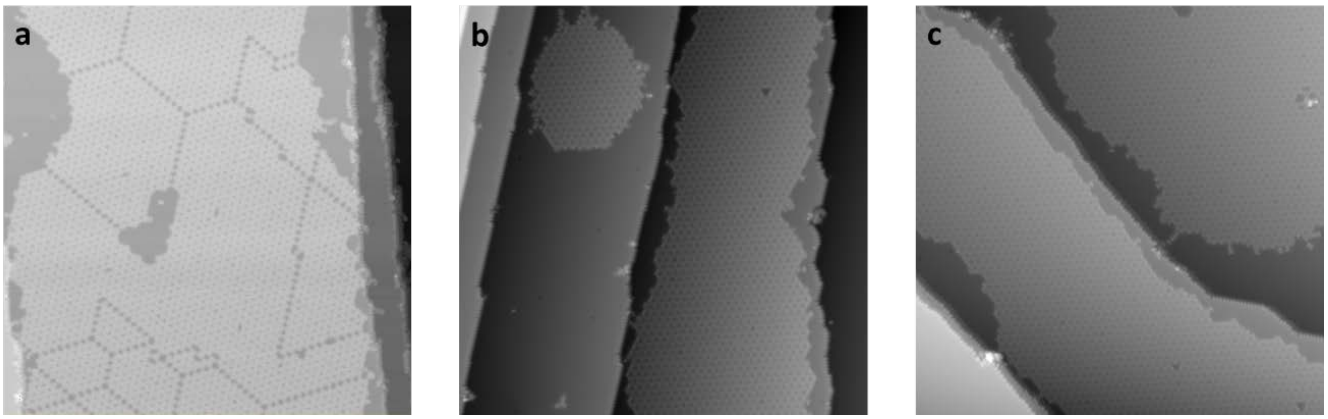

Fig. S1: STM overviews showing DCA-Cu network islands for unsaturated surfaces. STM parameters: all images are 100x100nm^2. a) 100pA; +1V; b) 100pA; -1V; c) 100pA; -1V.

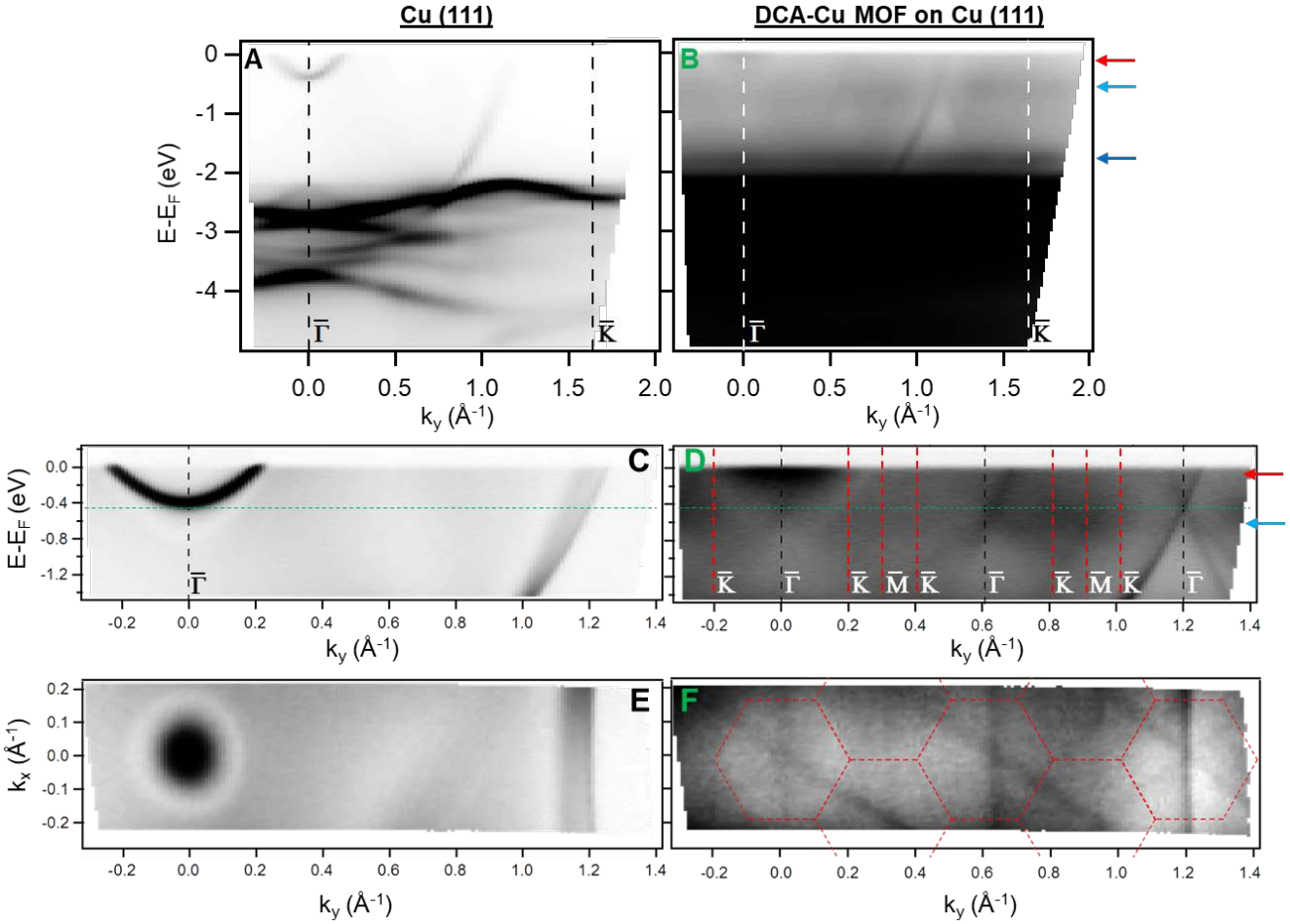

Fig. S2: ARPES signal comparison between the Cu(111) (left column) and the DCA-Cu network saturating the surface (right column) measured in our home lab. The band structure along the $\overline{\Gamma K}$ direction is shown in a large energy window that include the bulk d-bands in A) and B), whereas the region closer to the Fermi energy is displayed in C) and D). The high symmetry points are indicated as vertical lines. E) and F) contains an isoenegetic cut at 0.42 eV (marked by

the green, dotted horizontal line in the panels above), where the dotted hexagons exhibit the repeated Brillouin Zones. The side arrows indicate the network features discussed in the main text. ARPES details: Linear grayscales where darker corresponds to higher intensities. hν= 21.2 eV (He I_α), T_s = 150 K.

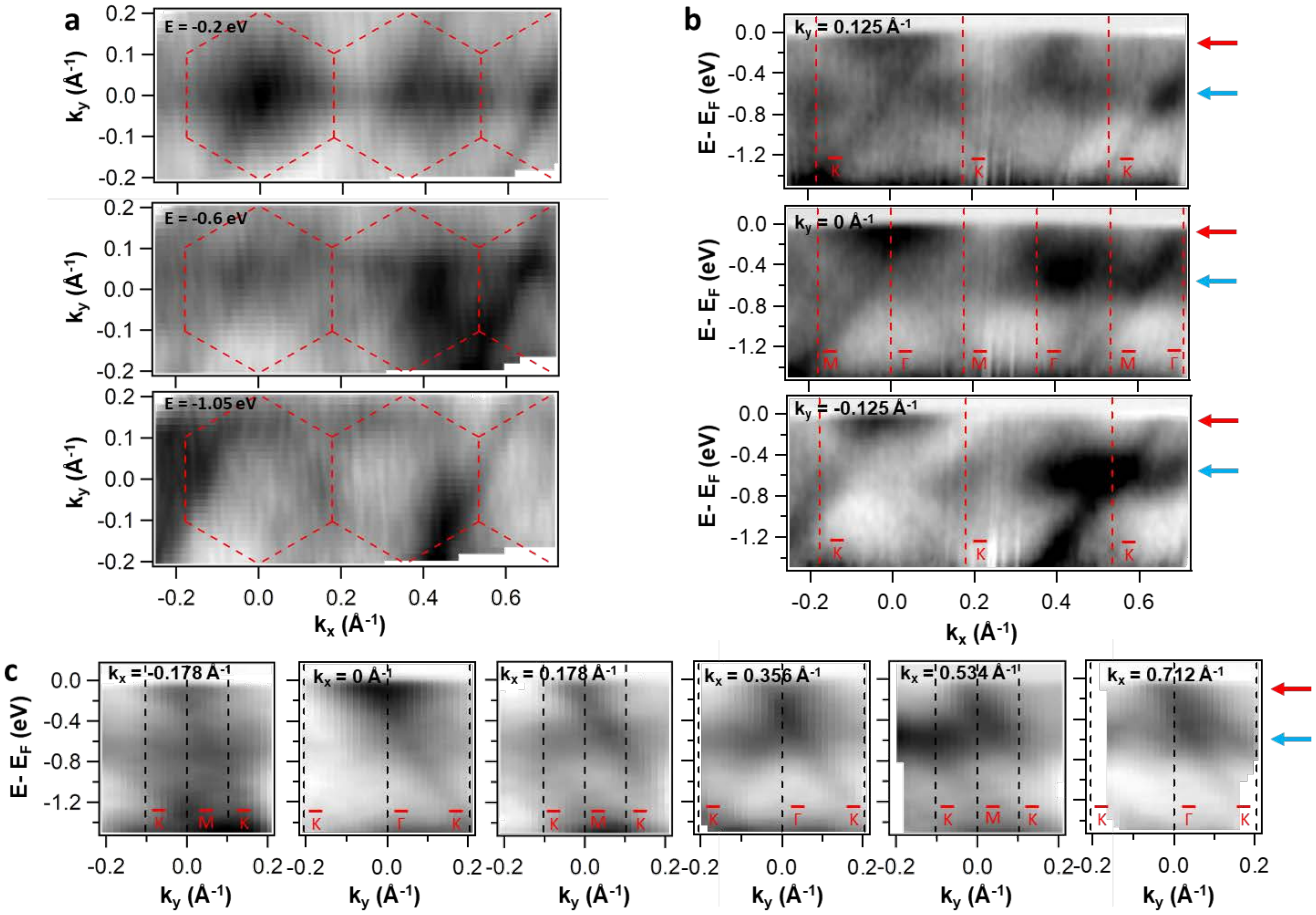

Fig. S3: Direct ARPES signal of a saturated surface of the DCA-Cu network measured in a synchrotron. a) Three different isoenergetic cuts at the energies indicated within each panel. The dotted hexagons indicate the repeated Brillouin Zones. b) Band structure parallel to the $\overline{\Gamma M}$ direction at selected k_y. c) Band structure cuts parallel to $\overline{\Gamma K}$ (perpendicular to b)) at the k_y values containing the high symmetry points. The side arrows indicate the network features discussed in the main text. ARPES details: Linear grayscales where darker corresponds to higher intensities. hν= 18 eV, T_s = 100 K.

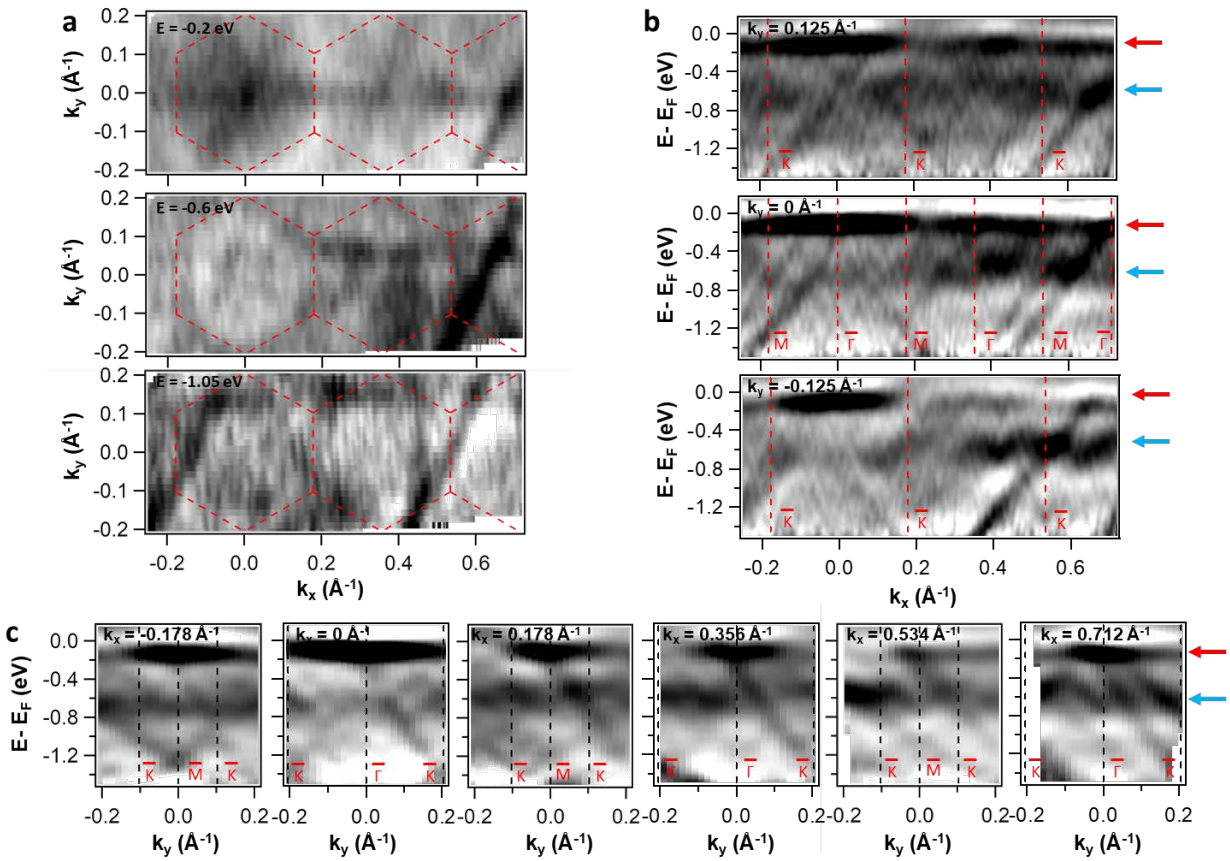

Fig. S4: Same as Fig. S3 but showing the 2nd derivative of the previous ARPES signal. The presence of the sp-bulk band umklapps hiders from a proper visualization of the network bands.

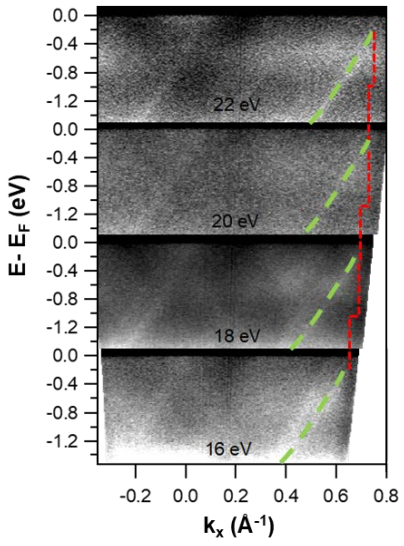

Fig. S5: Photon energy dependence of the band structure along the $\overline{\Gamma M}$ direction. The highly dispersive bands change their parallel momentum with photon energy (cf. the overimposed green discontinuous lines). Therefore, they must originate from sp-bulk band umklapps that appear by folding to the (8x8) of the network. Contrarily, the broad state at -0.6 eV does not shift, therefore it must have 2D origin, i.e. it is a network state. In the linear grayscale brighter corresponds to higher intensities.

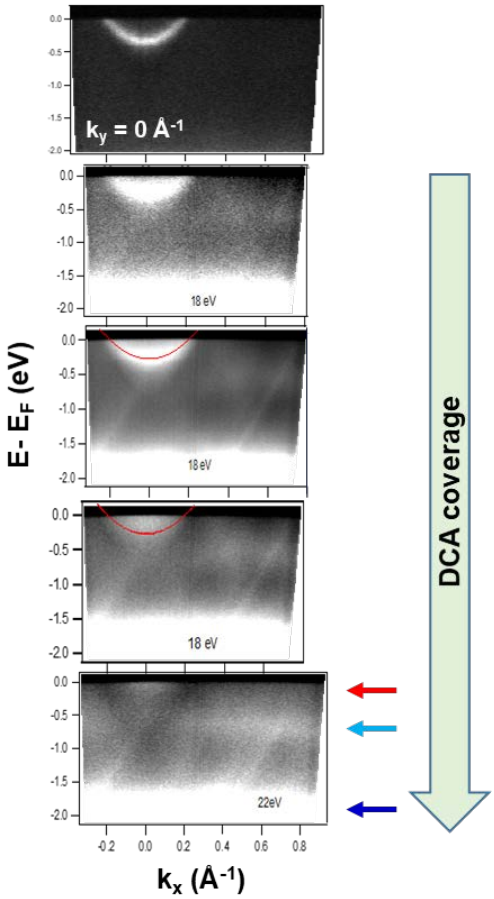

Fig. S6: Coverage dependent ARPES signal along the $\overline{\Gamma M}$ direction. The pristine Cu(111) is shown on the top panel and exhibits only the parabolic SS. Depositing DCA (increasing coverage from top to bottom) changes dramatically the ARPES signal (bright is more intense) so that highly dispersive umklapp bands stemming from the sp-bulk bands appear as well as the broad network band at -0.6 eV. Photon energies used hv= 22 eV and 18 eV, T_s = 100 K.

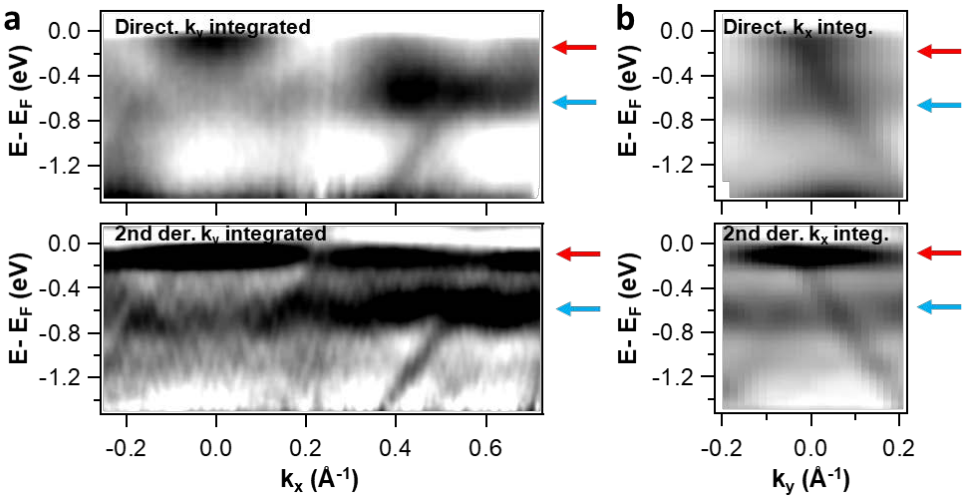

Fig. S7: Direct (top row) and 2nd derivative (bottom row) ARPES signal integrated along the $\overline{\Gamma M}$ (left column) and $\overline{\Gamma K}$ (right column) directions. The data clearly shows the broad network state at -0.6 eV. In the linear grayscale darker corresponds to higher intensities.

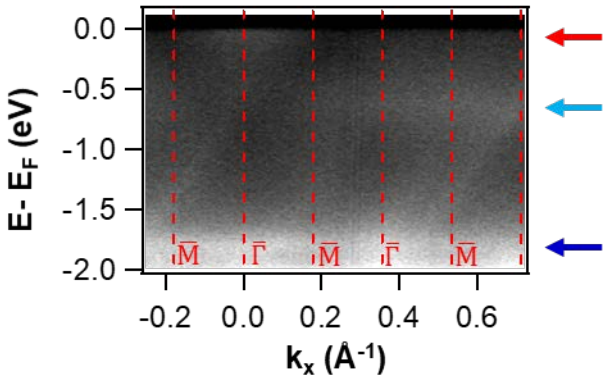

Fig. S8: Direct ARPES signal along the $\overline{\Gamma M}$ direction for a larger energy range. The grayscale (brighter corresponds to a more intense signal) shows three features indicated by the arrows that matches the STS peaks. Photon energy used hv= 22 eV with T_s = 100 K.

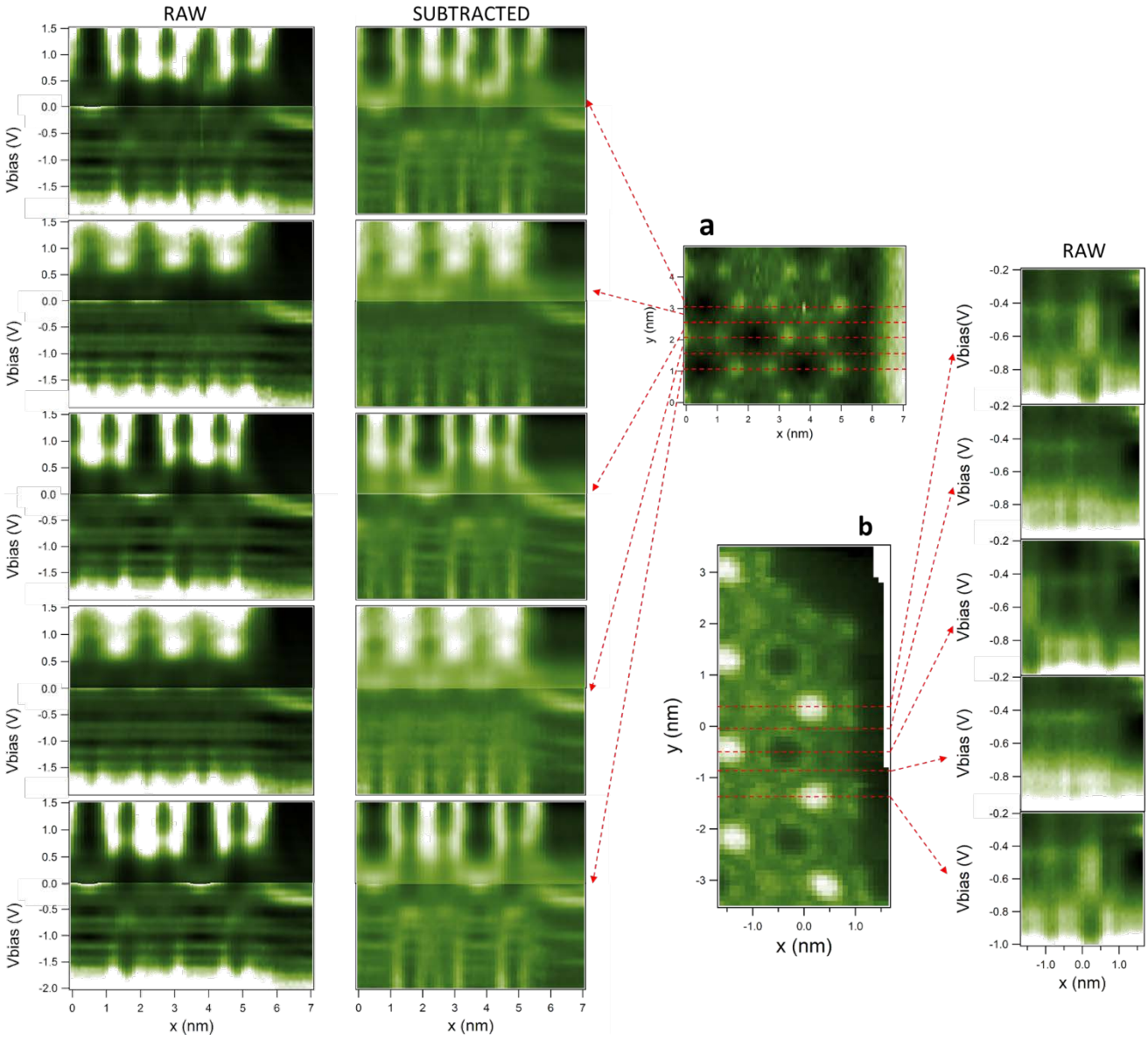

Fig. S9: dI/dV colorplots showing that no edge state develops. Data were extracted from two different dI/dV grids measured at two different regions. dI/dV maps of these regions are presented on the center and labeled as a) and b). On the side, five different horizontal line scans are selected from each grid, resulting in the dI/dV green colorplots (bright being more intense) as a function of position and V_{bias}. Note that in both panels, the first and the last horizontal lines are equivalent. In panel a), the intensity scale of the dI/dV colorplots are independent for positive and negative V_{bias} for better visualization. Intense tip states are detected in the occupied region (horizontal streaks), so the right column shows the data after subtraction at each grid point of an integrated dI/dV spectrum. With this subtraction, we visualize better the different features and reduce the tip state contribution. We observe the most important features described in the main text. The Cu(111) surface state is present at the substrate for voltages above -0.40 V. Close to the Fermi level (≈0 V) the confinement of the surface state in the pores is observed too. Two different types of Cu adatoms are distinguished at energies between -0.80 V and -0.50 V. We can find the molecular HOMO below -0.40 V localized at the external rings of the anthracenes of DCA, while the LUMO onset is observed at DCA centre at 0.50 V, which then peaks at 0.75V. This is a gap much smaller than the obtained by Liljeroth and coworkers for

metal-organic dimers on NaCl/Cu(111) [S2], which reported the HOMO at -0.76 V and the LUMO at 1.16 V. STS parameters: a) set point: I_t = 140 pA; V_{bias} = -1V; V_{rms} = 6.6mV; f_{osc} = 913Hz. Voltage range [-2V, 1.5V] b) I_t = 300pA; V_{bias} = -1V; V_{rms} = 9.6mV; f_{osc} = 817Hz. Voltage range [-1V, -0.2V]

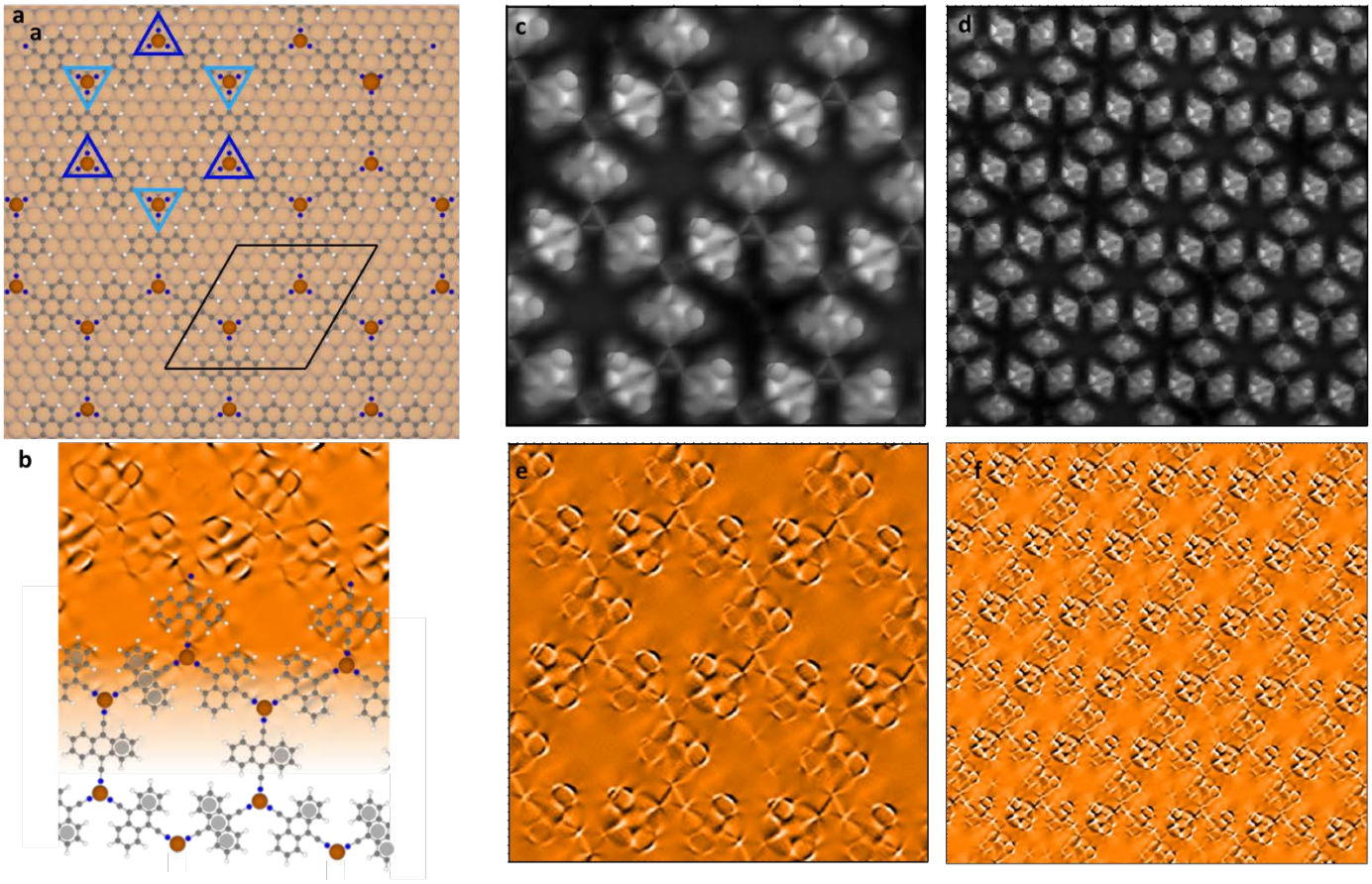

Fig. S10: a) Network model showing the perfect registry with the substrate. All anthracene rings are on top of surface atoms. Contrarily, the Cu adatoms are alternatively located in hcp and fcc sites, as marked by the different color triangles. b) Constant height image of the network and overlaid model (Image horizontal length: 4 nm). Two other constant height images of 5x5 nm^2 and 10x10 nm^2 showing the raw data in c), d) and the laplacian filtering in e) and f). The images b) and e) have been recorded in different preparations with different CO-functionalized tips. All show clear height differences in the molecules, where the protruding rings appear more defined.

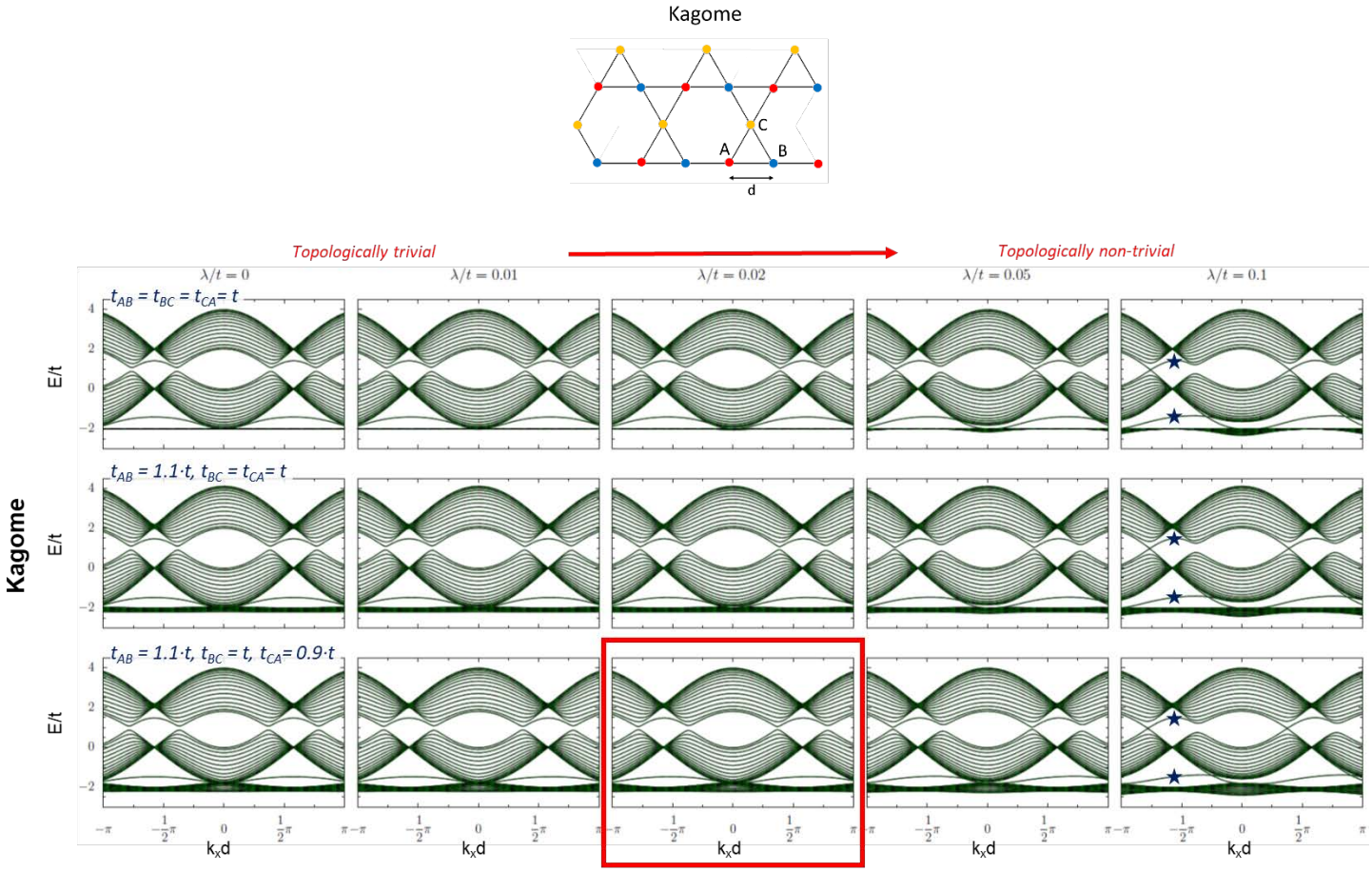

Fig. S11: First neighbor tight binding models for the kagome lattices projected into the island borders with varying ratio between the spin-orbit strength (λ) and hopping terms (*t*). The topologically trivial case always occurs for $\lambda/t = 0$, whereas the non-trivial topology of the kagome is displaced towards larger ratios. Indeed, protected edge states are visible always at $\lambda/t = 0.1$, as indicated by the dark blue stars. Note that the middle column ($\lambda/t = 0.02$) shows the OTI case reported in Ref. [S1]. The breaking of the network symmetry is qualitatively emulated here by introducing differences in the hopping values. Particularly, the red box highlights the case closest to our experimental case, where $t_{AB} = 1.1 \cdot t$, $t_{BC} = t$, $t_{CA} = 0.9 \cdot t$ and $\lambda/t = 0.02$, where no edge state develops.

SUPPLEMENTARY REFERENCES

[S1] L. Z. Zhang et al., *Intrinsic two-dimensional organic topological insulators in metal–dicyanoanthracene lattices*, Nano Lett. **16**, 2072 (2016).

[S2] P. Liljeroth, et al. *Single-Molecule Synthesis and Characterization of Metal–Ligand Complexes by Low-Temperature STM*, Nano Letters **10**, 2475 (2010).